Electronic Supplementary Material (ESI) for Chemical Communications.

Supporting Information for:

Optimizing $LiMn_{1.5}M_{0.5}O_4$ cathode materials for aqueous photo-rechargeable batteries

Kohei Shimokawa,*[ab] Shogo Matsubara,[c] Tomoya Kawaguchi,[b] Akihiro Okamoto[defg] and Tetsu Ichitsubo*[bh]

[a] *Frontier Research Institute for Interdisciplinary Sciences, Tohoku University, 6-3 Aramaki Aza Aoba, Aoba-ku, Sendai 980-8578, Japan*

[b] *Institute for Materials Research, Tohoku University, 2-1-1 Katahira, Aoba-ku, Sendai 980-8577, Japan*

[c] *Department of Life Science and Applied Chemistry, Graduate School of Engineering, Nagoya Institute of Technology, Gokiso-cho, Show-ku, Nagoya 466-8555, Japan*

[d] *International Center for Materials Nanoarchitectonics (WPI-MANA), National Institute for Materials Science, 1-1 Namiki, Tsukuba, Ibaraki 305-0044, Japan*

[e] *Research Center for Macromolecules and Biomaterials, National Institute for Materials Science, 1-1 Namiki, Tsukuba, 305-0044, Japan.*

[f] *Graduate School of Chemical Sciences and Engineering, Hokkaido University, North 13 West 8, Kita-ku, Sapporo, Hokkaido 060-8628, Japan*

[g] *Graduate School of Science and Technology, University of Tsukuba, 1-1-1 Tennodai, Tsukuba, 305-8577, Japan*

[h] *Advanced Science Research Center, Japan Atomic Energy Agency, 2-4 Shirakata, Tokai-mura, Naka-gun, Ibaraki 319-1195, Japan*

* *E-mail: kohei.shimokawa.b7@tohoku.ac.jp; tichi@imr.tohoku.ac.jp*

Methods

Materials synthesis. Spinel oxide materials were synthesized using a solution combustion method[S1,S2], as briefly described below. $LiNO_3$ (98%, Wako Pure Chemical Industries) and citric acid (98%, Wako Pure Chemical Industries) were dissolved in deionized water together with the following metal nitrates depending on the target materials: $Mn(NO_3)_2{\cdot}6H_2O$ (98%, Wako Pure Chemical Industries), $Fe(NO_3)_3{\cdot}9H_2O$ (99%, Wako Pure Chemical Industries), $Co(NO_3)_2{\cdot}6H_2O$ (99%, Wako Pure Chemical Industries), and $Zn(NO_3)_2{\cdot}6H_2O$ (99%, Wako Pure Chemical Industries). The mixing molar ratio was determined following the nominal composition of Li/Mn/*M* (*M* = Fe, Co, Ni, Zn) 1/1.5/0.5. The solution was heated by using a hot plate to obtain a gel, and then it was ignited by increasing the temperature. Although the materials after the combustion process were mostly oxide, they were further calcined in an air atmosphere to increase the crystallinity as well as to decrease the impurity phases. The materials were ground and then filtered to obtain fine powders. VESTA[S3] was used for the visualization of crystal structures.

Materials characterization. Powder X-ray diffraction (XRD) profiles were obtained by using an X-ray diffractometer (SmartLab, Rigaku) with Cu-*K*α radiation. Rietveld analysis was performed by using the RIETAN-FP program[S4]. Distributions of particle size were measured with a nanoparticle tracking analyser (NTA; ZetaView, Particle Metrix) and with scanning electron microscopy (SEM; JSM-7800F, JEOL). XRD measurements and SEM observation were carried out at the NIMS Battery Research Platform. Compositions of the synthesized materials were analyzed by inductively coupled plasma optical emission spectroscopy (ICP-OES) at the Analytical Research Core for Advanced Materials, Institute for Materials Research, Tohoku University. Energy-dispersive X-ray spectroscopy (EDS) was conducted by using SEM (JSM-7200F, JEOL) to investigate the distribution of particles in the composite electrodes. X-ray absorption near-edge structure (XANES) analysis was carried out at BL-12C, Photon Factory (PF), Japan. The materials after photocharging process were peeled off from the current corrector and then diluted with BN powder (99.5%, Mitsuwa Chemicals) for preparing pellets suitable for XANES measurements. The obtained profiles were analyzed using the Athena program[S5].

Electrochemical measurements. Composite electrodes were prepared to measure the electrochemical performance of the synthesized materials. Active material, carbon black (Super C65, Timcal), and polyvinylidene fluoride (PVdF) binder (KF Polymer L#7305, Kureha) were mixed in a weight ratio of 8/1/1. Anatase TiO_2 nanoparticles (JRC-TIO-10; reference catalyst, The Catalysis Society of Japan) was used for preparing the spinel oxide/TiO_2 mixed electrodes, where the weight ratio of spinel oxide/TiO_2 was fixed to 1 (*i.e.*, spinel oxide/TiO_2/carbon/PVdF = 4/4/1/1). Al foil was employed for the current corrector. Lithium bis(trifluoromethanesulfonyl)amide (LiTFSA; battery grade, Kishida Chemical) was dissolved in distilled water (HPLC grade, Sigma-Aldrich) to prepare the electrolyte of 21M LiTFSA/H_2O[S6]. Three-electrode beaker-type cells, as schematically illustrated in Fig. S9, were used for electrochemical experiments unless otherwise noted. Ag/AgCl in saturated KCl solution (EC Frontier) and Pt mesh (99.95%, Nilaco) were employed as the reference and counter electrodes, respectively. The area of the composite electrode was fixed to 1.0 cm^2, and the typical amount of the electrolyte was 4 mL. To investigate the electrochemical behavior under illumination, the working electrode in the beaker-type cell was illuminated by UV–visible light (300–600 nm) from a xenon lamp (MAX-350, Asahi Spectra), whose intensity was ~0.36 W/cm^2. Multichannel screen-printed electrodes (DropSens) were also used for evaluating various cathode materials at the same time. Small pieces of the composite electrode (~0.04 cm^2) were mounted on the Au working electrode with Al conductive tape. The counter and reference electrodes were Au and Ag pastes, respectively, and the typical amount of the electrolyte in each cell was 0.15 mL. Electrochemical impedance spectroscopy (EIS) and constant current charge/discharge test for $LiMn_{1.5}Fe_{0.5}O_4$ were carried out by using the beaker-type cell connected with a galvanostat/potentiostat (VSP, Biologic).

Photocharge/discharge test. The beaker-type cell (Fig. S9) was employed for the photocharge/discharge experiments. 50 mM $K_2S_2O_8$ (>99%, Sigma-Aldrich) was dissolved in 21 M LiTFSA/H_2O for photocharging, while 21 M LiTFSA/H_2O lacking $K_2S_2O_8$ was used for the following discharging process. The working electrode was illuminated with UV–visible light (300–600 nm; ~0.36 W/cm^2) from the xenon lamp, as described above, in the photocharging process to monitor the change in open-circuit potential (OCP). The photocharged electrodes were rinsed with distilled water and then used for the subsequent discharging tests to measure the capacity depending on the time of illumination in the photocharging process.

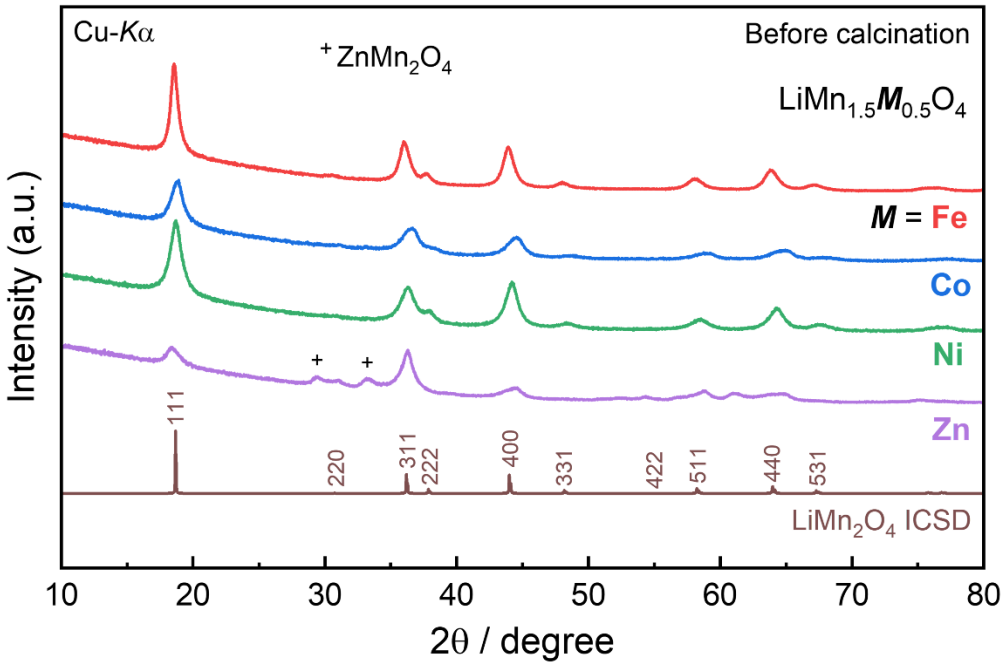

Figure S1. XRD profiles for the materials obtained via a solution combustion method. Although the obtained materials were mostly oxides, they were further calcined in a furnace to increase the crystallinity as well as to decrease the impurities, as shown in Figs. S2–S5.

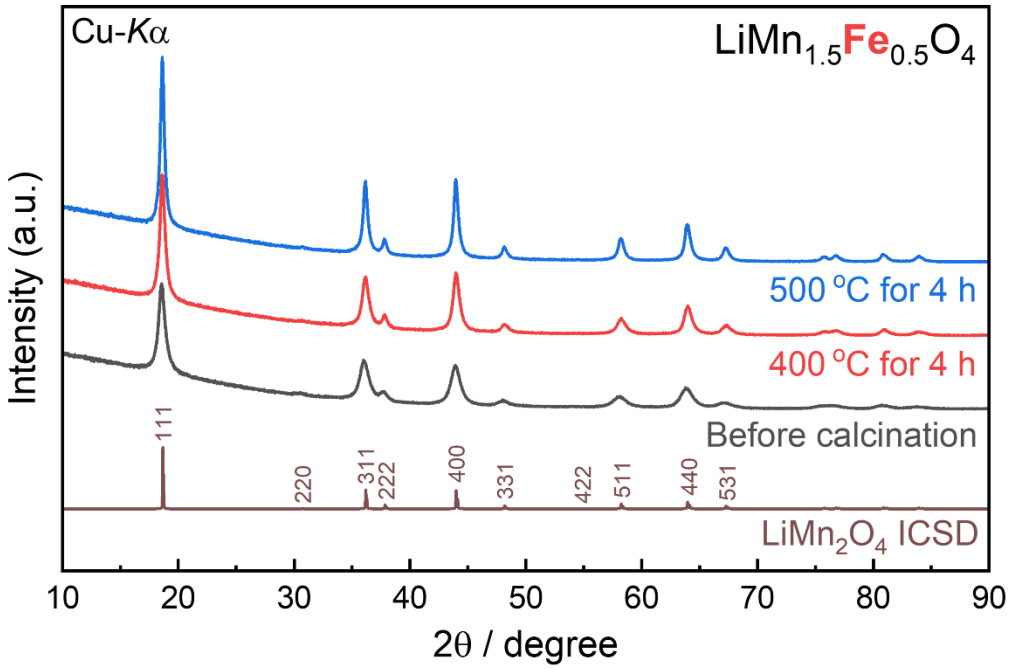

Figure S2. XRD profiles for the synthesized $LiMn_{1.5}Fe_{0.5}O_4$ nanoparticles after the calcination in an air atmosphere at 400 and 500 °C.

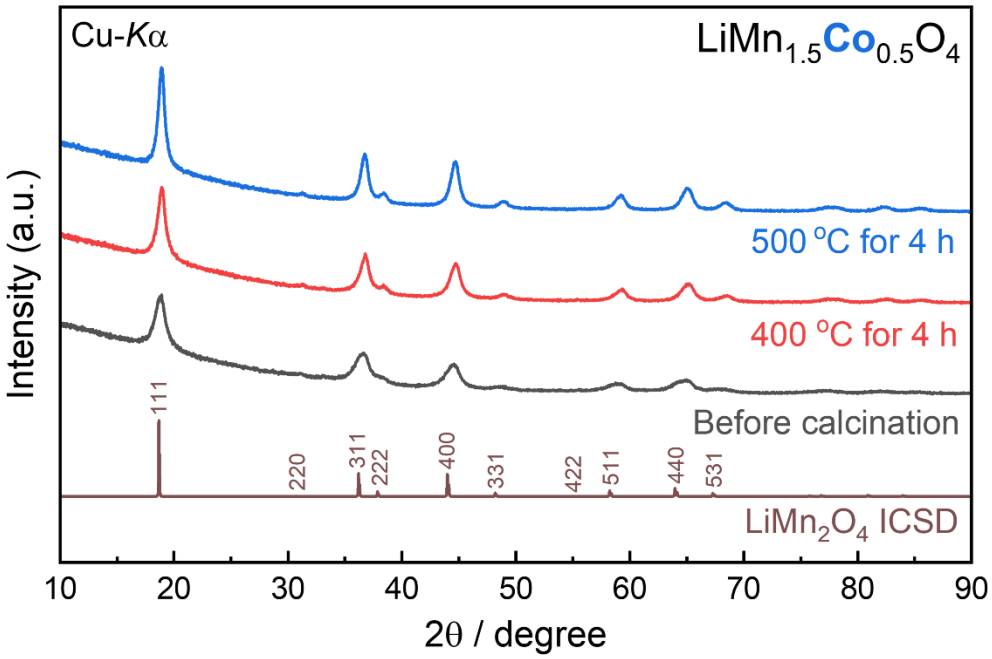

Figure S3. XRD profiles for the synthesized $LiMn_{1.5}Co_{0.5}O_4$ nanoparticles after the calcination in an air atmosphere at 400 and 500 °C.

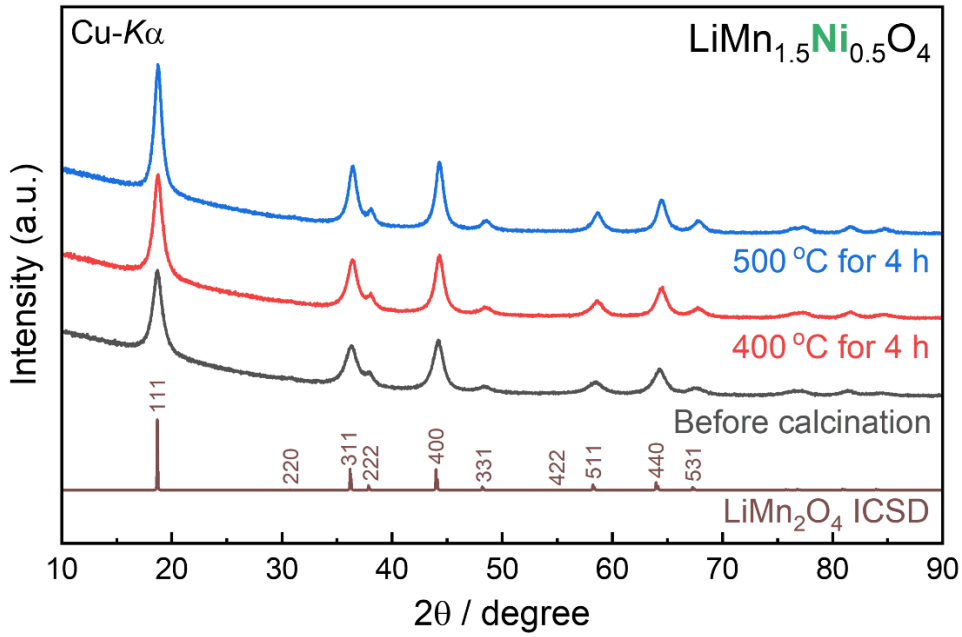

Figure S4. XRD profiles for the synthesized $LiMn_{1.5}Ni_{0.5}O_4$ nanoparticles after the calcination in an air atmosphere at 400 and 500 °C.

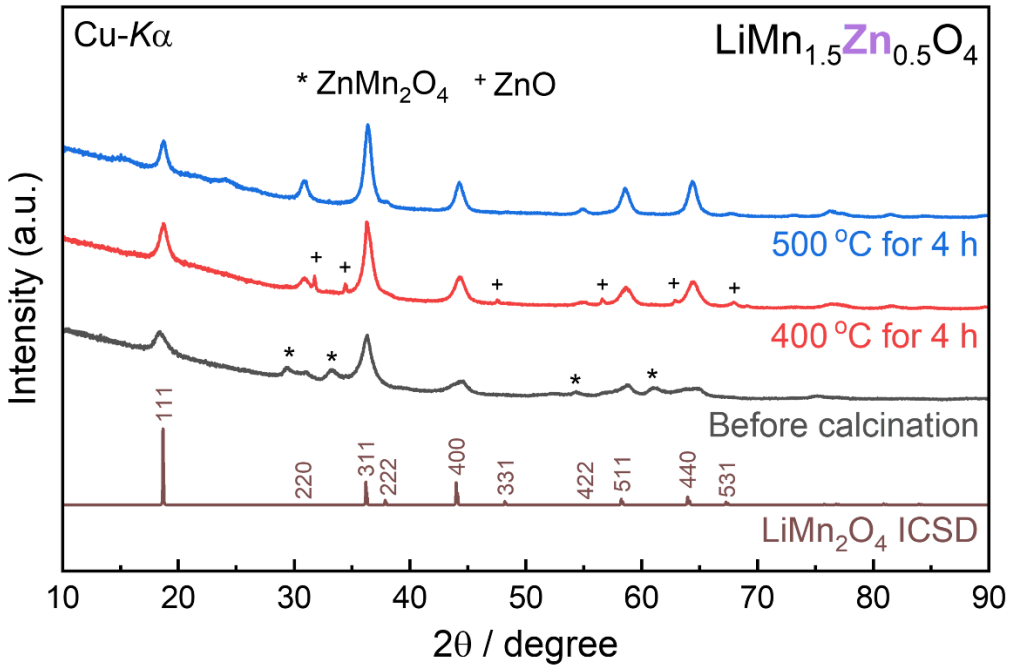

Figure S5. XRD profiles for the synthesized $LiMn_{1.5}Zn_{0.5}O_4$ nanoparticles after the calcination in an air atmosphere at 400 and 500 °C.

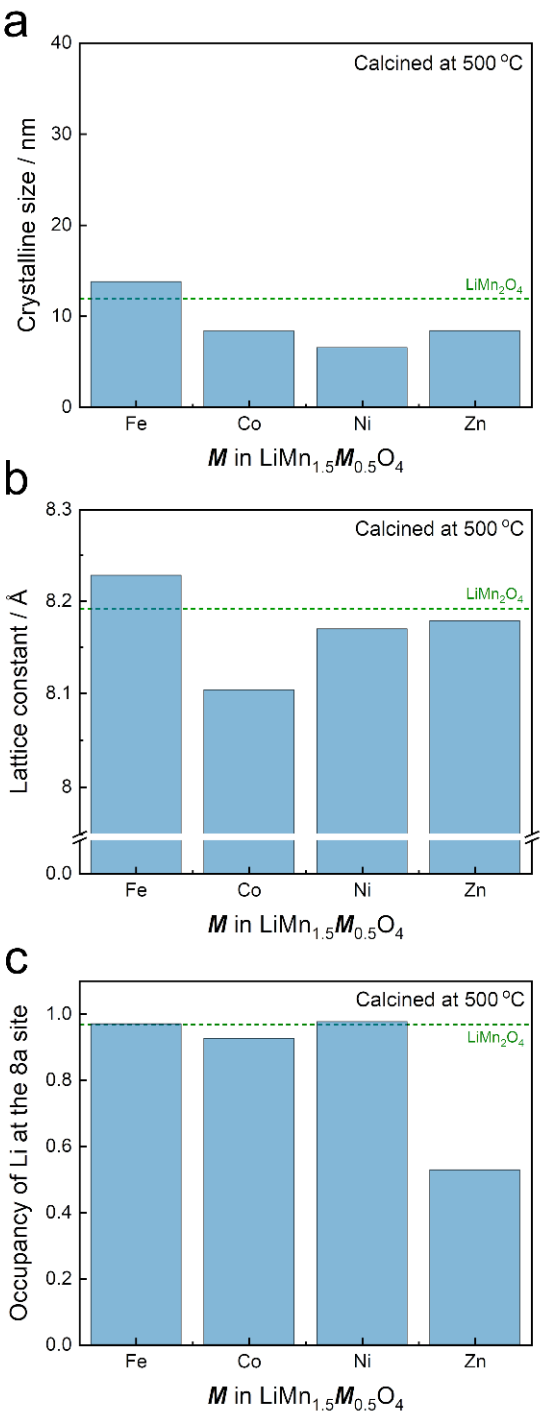

Figure S6. Summary of the results of Rietveld analysis for the materials after the calcination at 500 °C, showing the parameters of (a) crystalline size, (b) lattice constant, and (c) occupancy of Li at the 8a site. The values for $LiMn_2O_4$ determined in our previous report[S2] are also shown for comparison. The Rietveld analysis was carried out by using RIETAN-FP[S4] with the following constraints: (i) no vacancies at the 8a and 16d sites, (ii) the molar ratio of Li/Mn/*M* (*M* = Fe, Co, Ni, Zn) was fixed as the nominal composition, (iii) the location of Mn was fixed to the 16d site considering the result of our previous study[S2]. The obtained lattice constants were basically consistent with a previous report[S7]. A remarkable decrease in the occupancy of Li at the 8a site for $LiMn_{1.5}Zn_{0.5}O_4$ can be attributed to the strong preference of Zn for tetrahedral coordination in spinel oxides[S8].

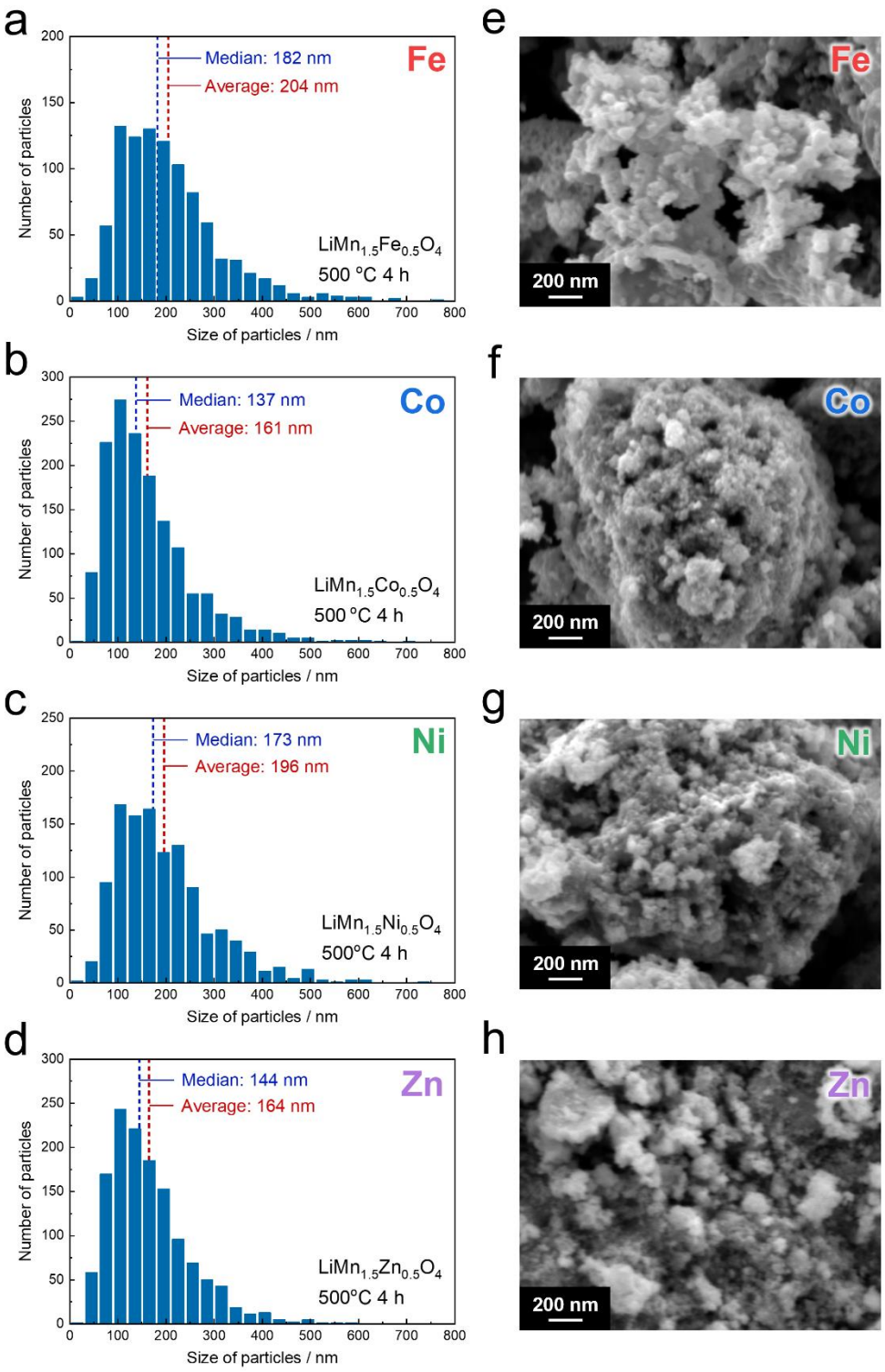

Figure S7. Distributions of the particle size measured with (a–d) NTA and (e–h) SEM for the synthesized $LiMn_{1.5}M_{0.5}O_4$ (M = Fe, Co, Ni, Zn) after calcination at 500 °C. All the scale bars are 200 nm.

Table S1. Compositions of $Li_xMn_{1.5}M_yO_4$ (M = Fe, Co, Ni, Zn) determined by ICP-OES. The values of x and y indicate the molar ratios of Li/1.5Mn and M/1.5Mn, respectively.

$Li_xMn_{1.5}M_yO_4$	x	y
M = Fe	1.00	0.49
M = Co	0.99	0.49
M = Ni	0.97	0.50
M = Zn	0.98	0.51

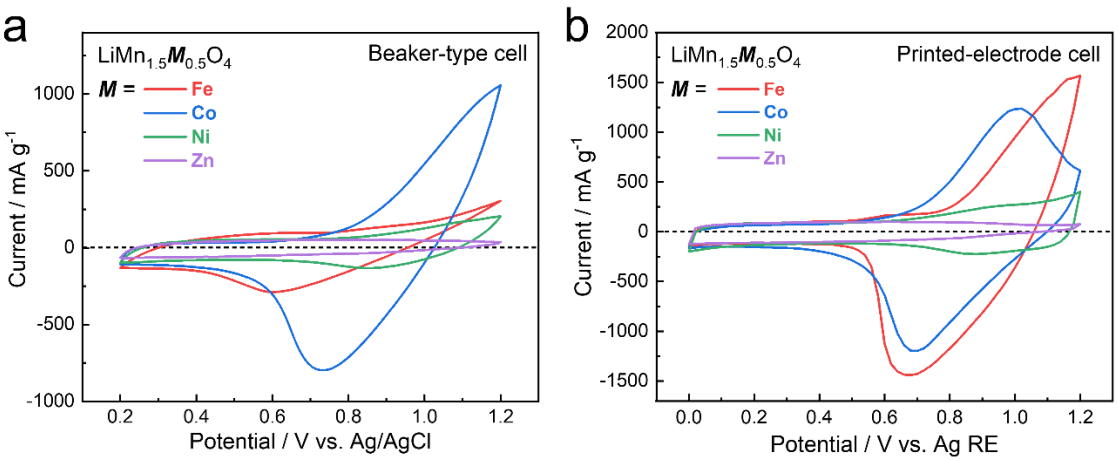

Figure S8. CV profiles of $LiMn_{1.5}M_{0.5}O_4$ (M = Fe, Co, Ni, Zn) obtained by using (a) beaker-type and (b) printed-electrode cells. In both measurements, the capacities of Fe- and Co-based materials were higher than those of Ni- and Zn-based materials, which is consistent with our basic strategy shown in Fig. 2a in the manuscript. The details of the profiles were different depending on the type of cells probably because both the size of working electrode and the volume of electrolyte were approximately 25 times higher in the beaker-type cell compared to those in the printed-electrode cell, as described in the Methods part.

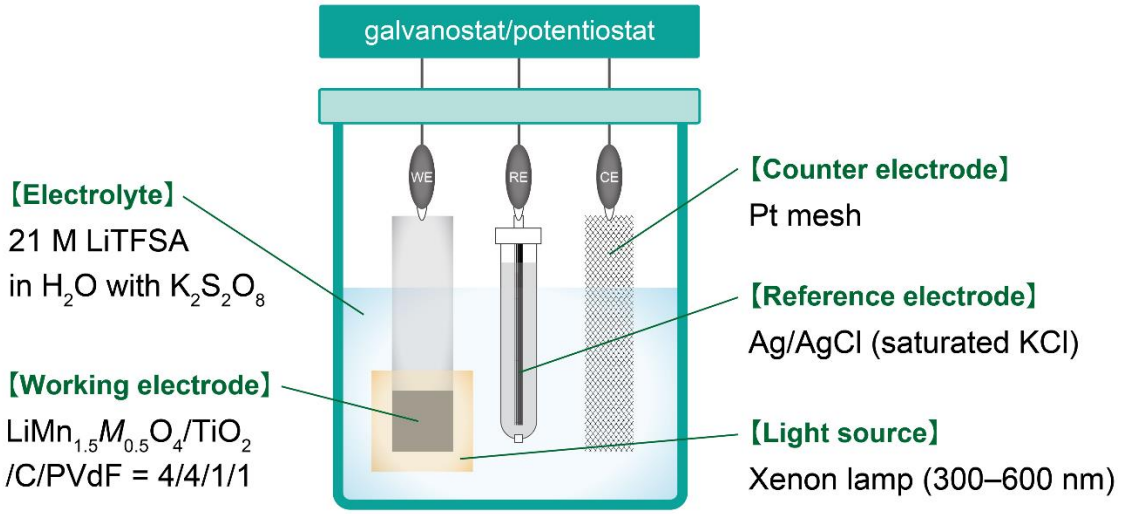

Figure S9. Schematic illustration showing the three-electrode beaker-type cell used for the photo-electrochemical measurements. The working electrode was a composite of spinel-oxide material, TiO_2 nanoparticles, carbon black, and PVdF binder, coated on an Al foil. The composite was illuminated by UV–visible light from a xenon lamp. 21 M LiTFSA/H_2O with 50 mM $K_2S_2O_8$ as an electron acceptor was employed for the electrolyte, as well as in our previous work[S2].

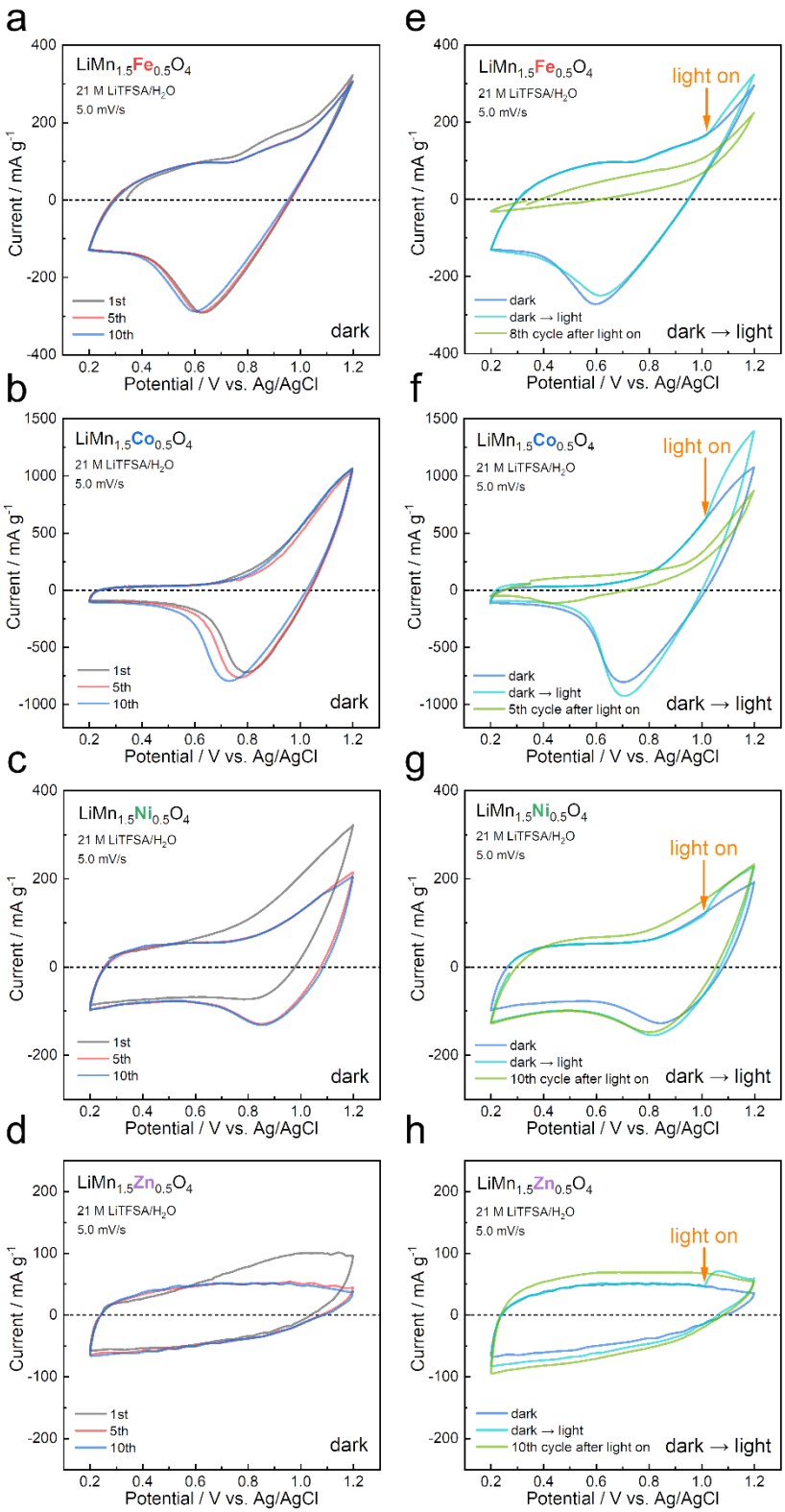

Figure S10. CV profiles for the electrode of $LiMn_{1.5}M_{0.5}O_4$ (M = Fe, Co, Ni, Zn) (a–d) in dark and (e–h) after illumination.

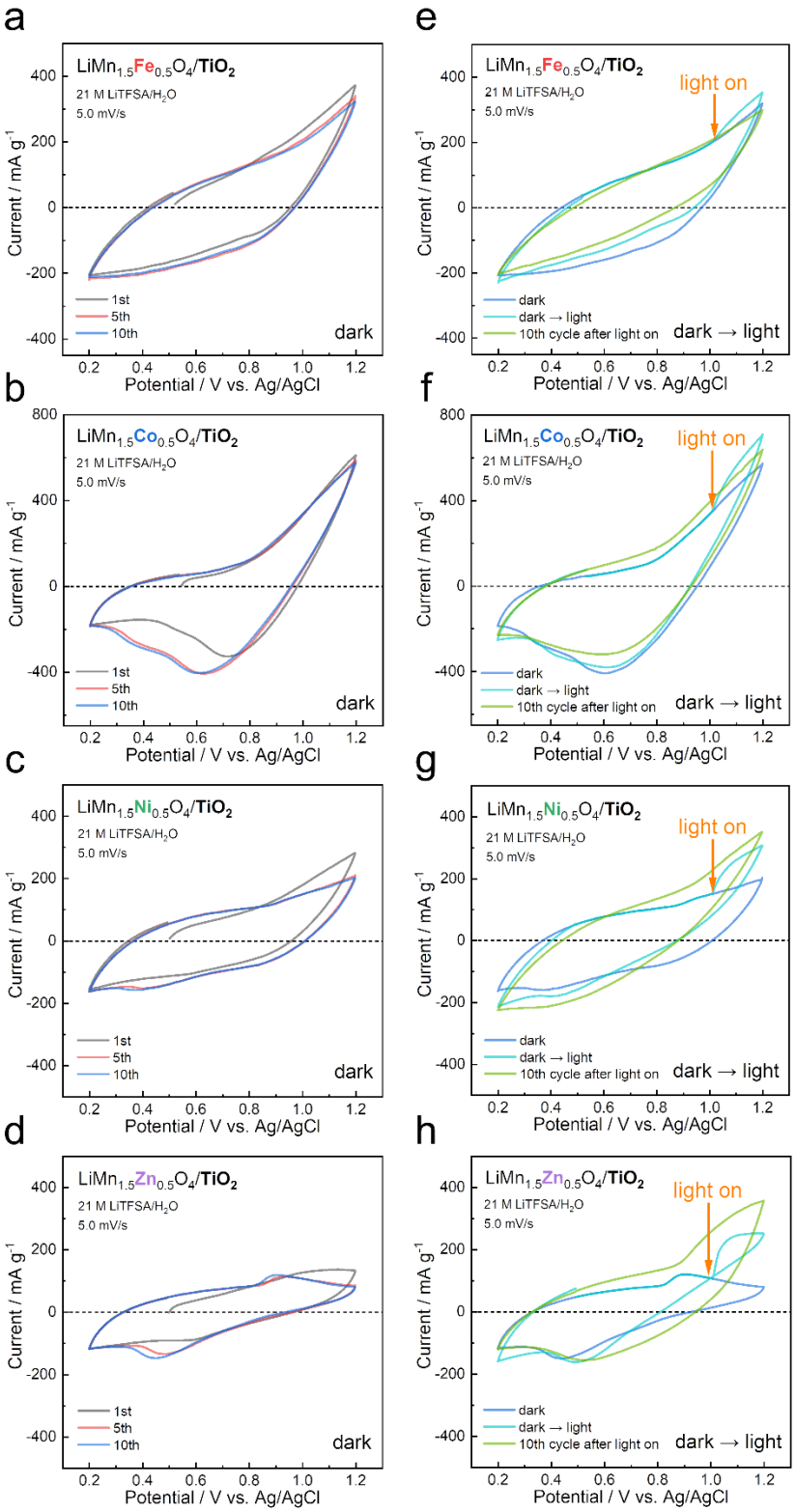

Figure S11. CV profiles for the electrode of $LiMn_{1.5}M_{0.5}O_4/TiO_2$ (M = Fe, Co, Ni, Zn) (a–d) in dark and (e–h) after illumination.

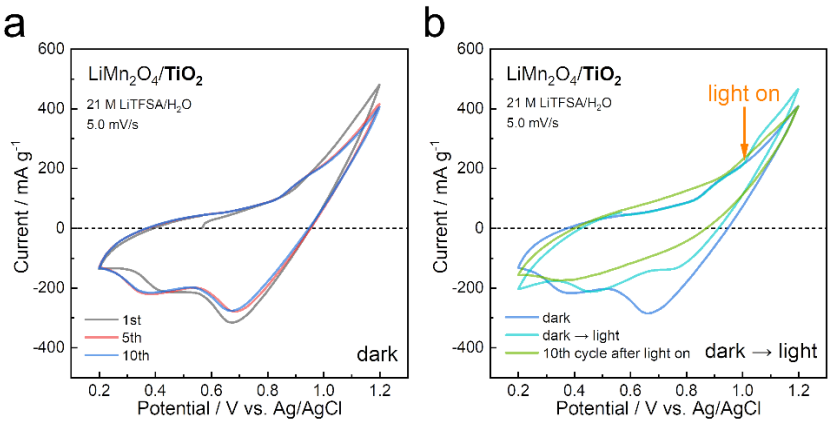

Figure S12. CV profiles for the electrode of $LiMn_2O_4/TiO_2$ (a) in dark and (b) after illumination.

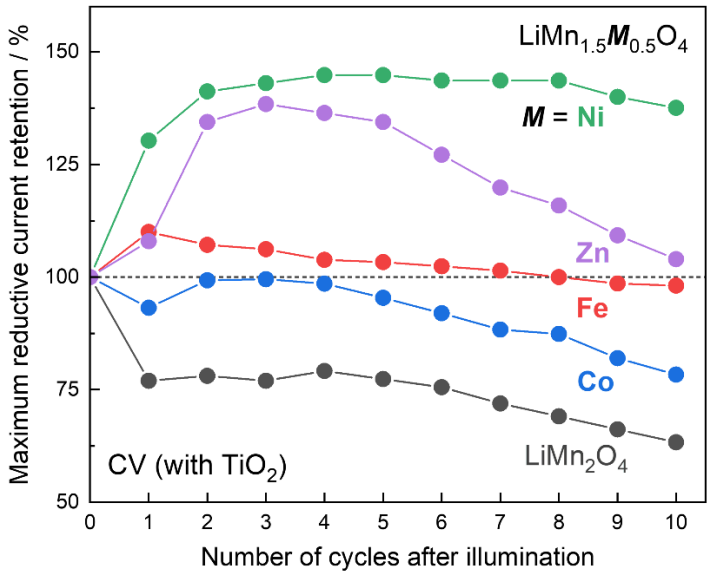

Figure S13. Maximum reductive current retention in CV measurements after illumination. The values for $LiMn_{1.5}M_{0.5}O_4$ (M = Fe, Co, Ni, Zn) were higher than those of $LiMn_2O_4$, indicating enhanced stability under illumination by partial substitution of Mn with other elements.

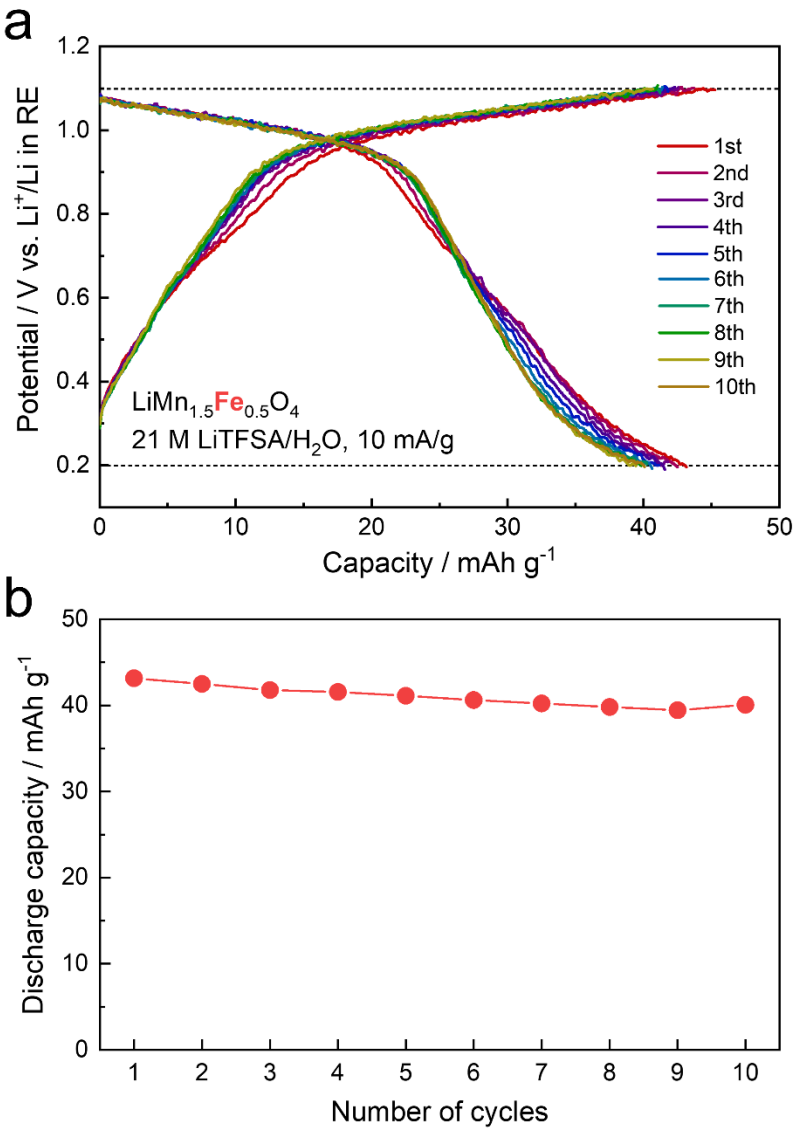

Figure S14. (a) Constant current charge/discharge profiles for $LiMn_{1.5}Fe_{0.5}O_4$ (with TiO_2) measured in the dark condition and (b) its capacity retention, where the electrolyte was 21 M LiTFSA/H_2O. Note that the capacity was limited due to the relatively low charging cut-off potential (1.1 V vs. Ag/AgCl).

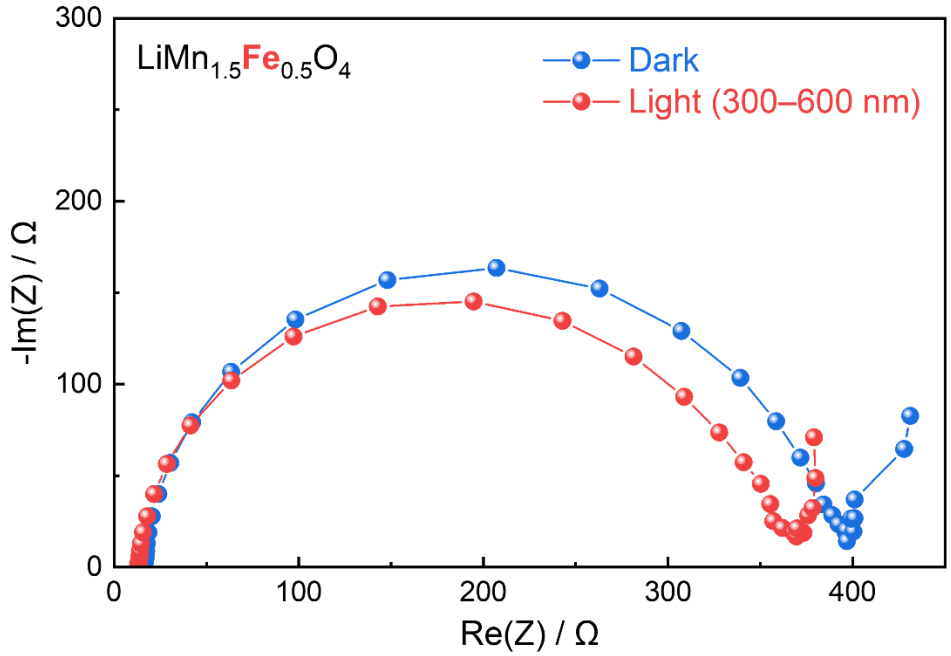

Figure S15. Electrochemical impedance spectra for the electrode of $LiMn_{1.5}Fe_{0.5}O_4$ (without TiO_2) under the dark and light conditions in the frequency range from 100 mHz to 100 kHz at 10 mV amplitude. The material was discharged state after CV cycles in the electrolyte of 21 M LiTFSA/H_2O. The charge-transfer resistance decreased under UV–visible light illumination.

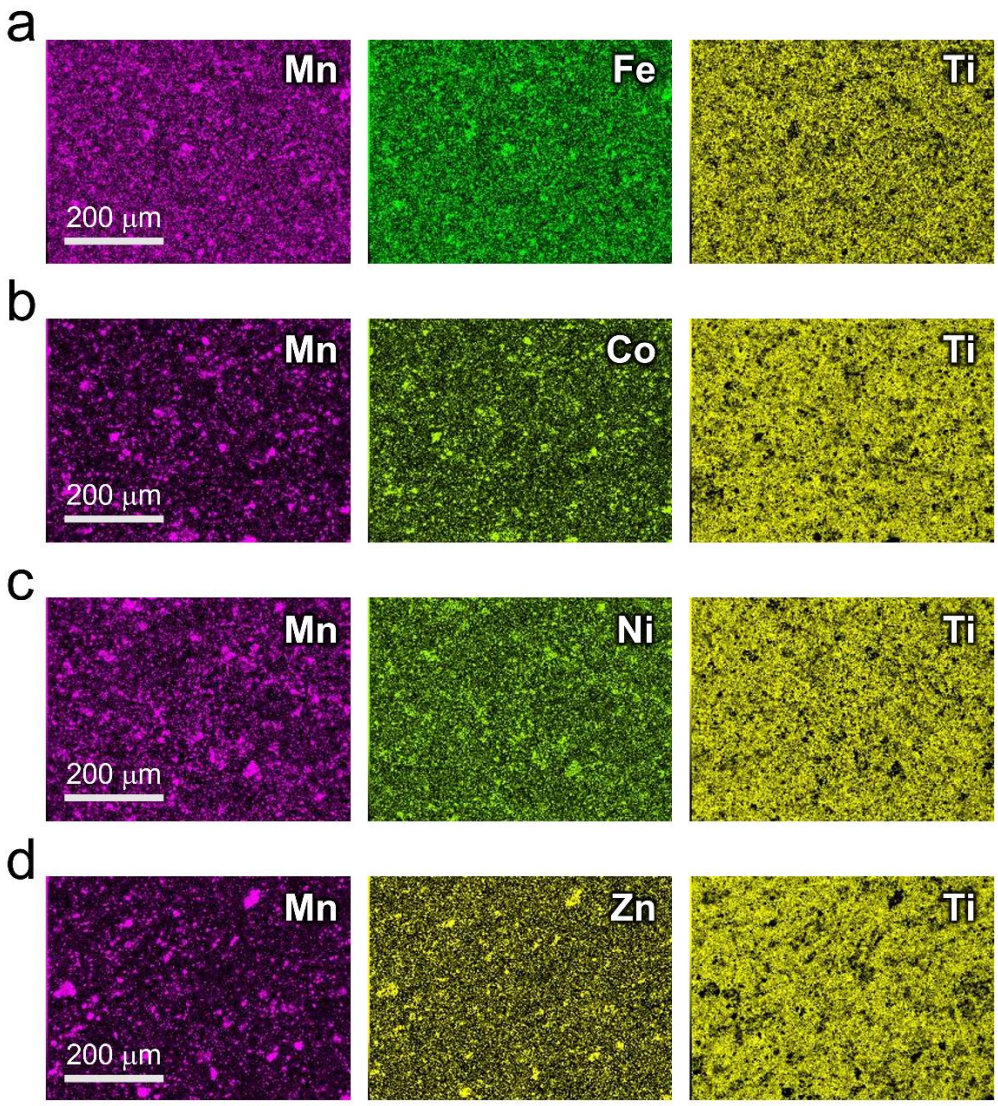

Figure S16. EDS mapping results for the composite electrodes of $LiMn_{1.5}M_{0.5}O_4/TiO_2$, where *M* is (a) Fe, (b) Co, (c) Ni, and (d) Zn. Although some amounts of coarse particles were observed for $LiMn_{1.5}M_{0.5}O_4$, TiO_2 nanoparticles were homogeneously distributed in each electrode. All the scale bars are 200 μm.

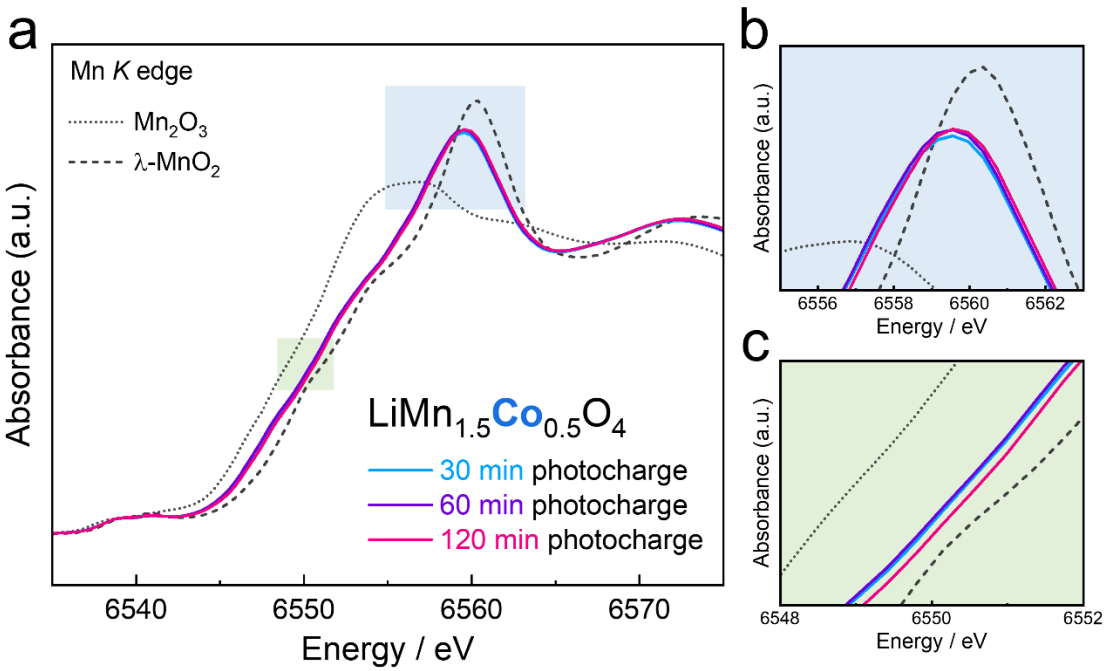

Figure S17. (a) Mn *K*-edge XANES profiles of $LiMn_{1.5}Co_{0.5}O_4$ after photocharging, together with those of Mn_2O_3 and λ-MnO_2 for comparison, and (b,c) enlarged views. The edge shift was much smaller than that for $LiMn_{1.5}Fe_{0.5}O_4$ (Fig. S18), which is consistent with the discharge capacities after the photocharging process shown in Fig. 4 in the manuscript.

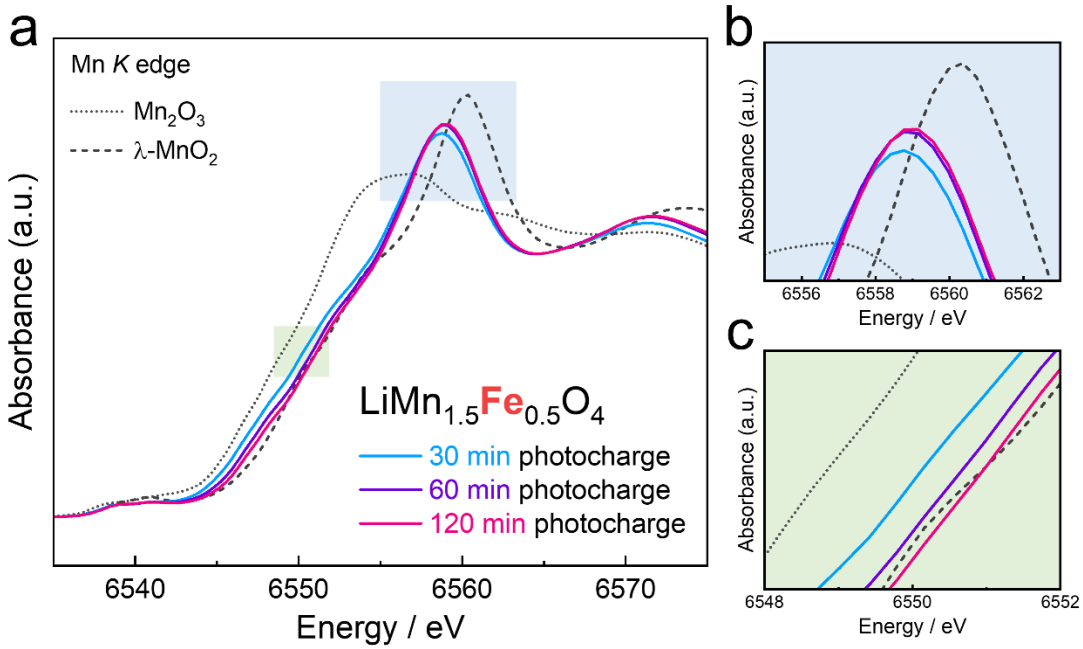

Figure S18. (a) Mn *K*-edge XANES profiles of $LiMn_{1.5}Fe_{0.5}O_4$ after photocharging, together with those of Mn_2O_3 and λ-MnO_2 for comparison, and (b,c) enlarged views. The edge shift toward higher energy depending on the time of illumination was clearly observed, indicating the oxidation of Mn in the material during the photocharging process.

References:

[S1] A. Varma, A. S. Mukasyan, A. S. Rogachev and K. V. Manukyan, Solution combustion synthesis of nanoscale materials. *Chem. Rev.*, **116**, 14493−14586 (2016).

[S2] K. Shimokawa, S. Matsubara, A. Okamoto and T. Ichitsubo, Light-induced Li extraction from $LiMn_2O_4/TiO_2$ in a water-in-salt electrolyte for photo-rechargeable batteries. *Chem. Commun.*, **58**, 9634−9637 (2022).

[S3] K. Momma and F. Izumi, VESTA 3 for three-dimensional visualization of crystal, volumetric and morphology data. *J. Appl. Crystallogr.*, **44**, 1272−1276 (2011).

[S4] F. Izumi and K. Momma, Three-dimensional visualization in powder diffraction. *Solid State Phenom.*, **130**, 15−20 (2007).

[S5] B. Ravel and M. Newville, ATHENA, ARTEMIS, HEPHAESTUS: data analysis for X-ray absorption spectroscopy using IFEFFIT. *J. Synchrotron Radiat.*, **12**, 537−541 (2005).

[S6] L. Suo, O. Borodin, T. Gao, M. Olguin, J. Ho, X. Fan, C. Luo, C. Wang and K. Xu, "Water-in-salt" electrolyte enables high-voltage aqueous lithium-ion chemistries. *Science*, **350**, 938−943 (2015).

[S7] J. C. Knight, S. Therese and A. Manthiram, Delithiation mechanisms in acid of spinel $LiMn_{2-x}M_xO_4$ (M = Cr, Fe, Co, and Ni) cathodes. *J. Electrochem. Soc.*, **162**, A426−A431 (2015).

[S8] K. Shimokawa, T. Atsumi, M. Harada, R. E. Ward, M. Nakayama, Y. Kumagai, F. Oba, N. L. Okamoto, K. Kanamura and T. Ichitsubo, Zinc-based spinel cathode materials for magnesium rechargeable batteries: toward the reversible spinel–rocksalt transition. *J. Mater. Chem. A*, **7**, 12225−12235 (2019).